RESEARCH LETTER

Key Points:
- Rigid plate motions, coupled with line-of-sight variation, introduce long-wavelength spatial gradients in Interferometric Synthetic Aperture Radar (InSAR)-derived velocity maps
- Plate motion effects dominate the long-wavelength components in InSAR velocities after ionospheric correction
- Plate motion effects can be easily accounted for using plate motion models, improving long-wavelength deformation mapping from InSAR

Oliver L. Stephenson and Yuan-Kai Liu contributed equally to this work.

The Impact of Plate Motions on Long-Wavelength InSAR-Derived Velocity Fields

Oliver L. Stephenson[1] [iD], **Yuan-Kai Liu**[1] [iD], **Zhang Yunjun**[1] [iD], **Mark Simons**[1] [iD], **Paul Rosen**[2] [iD], and **Xiaohua Xu**[3] [iD]

[1]Seismological Laboratory, Division of Geological and Planetary Sciences, California Institute of Technology, Pasadena, CA, USA, [2]Jet Propulsion Laboratory, California Institute of Technology, Pasadena, CA, USA, [3]Institute for Geophysics, University of Texas at Austin, Austin, TX, USA

Abstract Interferometric Synthetic Aperture Radar (InSAR) measurements are increasingly being used to measure small amplitude tectonic deformations over large spatial scales. Residual signals are often present at these scales and are interpreted to be noise of indeterminate origin, limiting studies of long-wavelength deformation. Here, we demonstrate the impact of rigid motion by the Earth's tectonic plates on velocity fields derived from InSAR. The range-dependent incidence angle of the InSAR observations, coupled with plate velocities of centimeters per year, can induce long-wavelength spatial gradients of millimeters per year over hundreds of kilometers in InSAR velocity fields. We show that, after applying corrections, including for the ionosphere and troposphere, plate motion represents the dominant source of long-wavelength secular velocity gradients in multi-year time series for several study areas. This signal can be accounted for using plate motion models, allowing improved detection of regional tectonic strain at continental scales.

Plain Language Summary Radar interferometry from repeat satellite images has been used to measure slow motions of the Earth's surface. These motions could help us understand a range of processes happening at and below the surface, from hydrology to tectonics. We show how the rigid motion of Earth's tectonic plates can create a ramp effect in InSAR data that may obscure long-wavelength deformation signals of interest. We demonstrate a simple method for removing this ramp effect, making InSAR more useful for studying very small motions over large areas of the Earth, especially in regions where we do not have good observations from other sources.

1. Introduction

Interferometric Synthetic Aperture Radar (InSAR) is an active imaging technique for measuring ground displacements that occur between repeat passes of an imaging platform, such as a satellite (e.g., Hanssen, 2001; Massonnet & Feigl, 1998; Simons & Rosen, 2015). InSAR deformation measurements are generally expressed relative to a single point, or ensemble of points, within the imaged area, usually assumed be stable through time (e.g., Mahapatra et al., 2018). While InSAR has been used extensively for measuring large amplitude (>1 cm) deformation over short wavelengths (<100 km) (e.g., Massonnet et al., 1993; Merryman Boncori, 2019), other signals and errors present in the data challenge our ability to measure deformation at the scale of millimeters per year over hundreds of kilometers (e.g., Fournier et al., 2011; Parizzi et al., 2021).

InSAR observations at long wavelengths are the combination of motion of the Earth's surface, changes in the atmosphere, and measurement and processing errors. The Earth motion signals comprise the surface deformation of interest, for example, from tectonic strain, volcanic activity, or subsidence (Amelung et al., 1999; Massonnet et al., 1993; Massonnet & Feigl, 1998), along with solid Earth tides (SET) (Xu & Sandwell, 2020), and ocean tidal loading (DiCaprio & Simons, 2008). Atmospheric signals come from propagation delay through the ionosphere (Z.-W. Xu et al., 2004) and troposphere (Tarayre & Massonnet, 1996), while error sources include satellite orbits (Massonnet & Feigl, 1998), local oscillator drift (Marinkovic & Larsen, 2015), phase unwrapping (Biggs et al., 2007), and topography (Berardino et al., 2002).

It is challenging to separate small, long-wavelength deformation due to local tectonic processes from the other effects described above. Thus, it is common to not interpret long-wavelength signals from InSAR alone, instead removing them by empirically fitting 2D polynomial functions, known as "ramps," to the data (e.g., Fialko, 2006; Jolivet et al., 2015), or combining InSAR velocities with Global Navigation Satellite System

(GNSS) measurements in order to constrain the deformation at large spatial scales (e.g., Weiss et al., 2020; X. Xu et al., 2021; Neely et al., 2020; Parizzi et al., 2020). Such approaches are limiting when we wish to measure large-scale deformation in regions with sparse GNSS coverage (Chaussard et al., 2016; Neely et al., 2020).

The quality of InSAR data and correction methods have substantially increased over the last several years. The European Space Agency's (ESA) Sentinel-1 satellites have been regularly acquiring data for significant portions of the planet since late 2014. Sentinel-1 offers the advantages of improved orbital controls and uncertainties compared to earlier satellite missions, reducing the noise contribution from satellite orbits (Fattahi & Amelung, 2014; Peter, 2021), as well as unrestricted data access. Split-band processing now allows for the estimation of the ionospheric signal directly from the InSAR data (Fattahi, Simons, & Agram, 2017; Gomba et al., 2016; Liang et al., 2019), and higher-quality weather models have improved the correction of the tropospheric phase (Doin et al., 2009; Jolivet et al., 2011; Li et al., 2005). Techniques for removing the SET (Xu & Sandwell, 2020; Yunjun et al., 2022) and ocean tidal loading signals (DiCaprio & Simons, 2008; Yu et al., 2020) have also been developed, among other correction methods. After corrections, there may still be long-wavelength residuals in multi-year Sentinel-1 time series, including from the troposphere, which can contribute up to 5 mm/yr over 150 km (Parizzi et al., 2021), and orbital errors, contributing around 0.5 mm/yr over 100 km for Sentinel-1 (Fattahi & Amelung, 2014).

In this work, we focus on another component of long-wavelength InSAR-derived velocity fields: the rigid motion of Earth's tectonic plates. The satellite line-of-sight (LOS) vector varies systematically in the range (across-track) direction, causing a range-dependent sensitivity to ground displacement. The rigid motion of tectonic plates in the satellite frame of reference, coupled with this LOS variation, can create quasi-linear gradients (ramps) in InSAR velocity fields, predominantly in the satellite range direction. Because of this effect, it is important to consider the reference frame of InSAR observations before interpreting the results.

Several authors have investigated the reference frame of InSAR observations, generally in the context of using GNSS to put InSAR measurements into a terrestrial reference frame (e.g., Johnston et al., 2021; Mahapatra et al., 2018). Bähr et al. (2012) and Bähr (2013) noted that plate motion would affect InSAR measurements, and that this could be accounted for using a temporally increasing correction to the interferometric baseline. However, the size of the plate motion signal was too small to be seen with the quality of data available at the time. Parizzi et al. (2020) used a plate motion model (PMM) to adjust their LOS velocity fields after merging InSAR with GNSS. Authors have also noted the impact of plate motions on SAR geolocation accuracy (Cong et al., 2012).

Here, we demonstrate that, after other corrections have been applied, plate motions can explain a significant fraction of observed residual long-wavelength surface velocities of several millimeters per year, across the 250 km track width, in six multi-year Sentinel-1 InSAR time series. We show that this residual can be straightforwardly compensated for using plate motion models without combining InSAR data with GNSS. This adjustment is not currently part of several open-source InSAR time series analysis packages (e.g., Agram et al., 2013; Hooper et al., 2012; Morishita et al., 2020; Yunjun et al., 2019), and we provide an implementation of the adjustment in the MintPy package (Yunjun et al., 2019).

2. The Reference Frame of InSAR Measurements

Quantifying ground deformation using InSAR requires a precise measurement of the satellite orbit ephemerides (Fattahi & Amelung, 2014; Peter, 2021). For Sentinel-1 the orbit is measured with respect to the International Terrestrial Reference Frame 2014 (ITRF2014, abbreviated as ITRF) (Peter, 2021), an Earth-centered, Earth-fixed reference frame in which there is no net rotation of the Earth's surface (Altamimi et al., 2016). Observations of absolute ground motion relative to the satellite are therefore also in ITRF (Bähr et al., 2012; Lazecky & Hooper, 2022).

However, it is not possible for InSAR to record absolute motions due to the 2π ambiguity in the interferometric phase (e.g., Massonnet & Feigl, 1998). Instead, displacement measurements are generally expressed relative to a reference point within the imaged region, assumed to be stationary. Velocities can then be obtained from functional fits to displacement time series, with inferred velocities also expressed relative to the reference point.

Selecting the reference point is not equivalent to expressing the InSAR velocities in a reference frame moving with that point (Bähr, 2013; Bähr et al., 2012). Thus, referencing InSAR velocities does not remove the effect
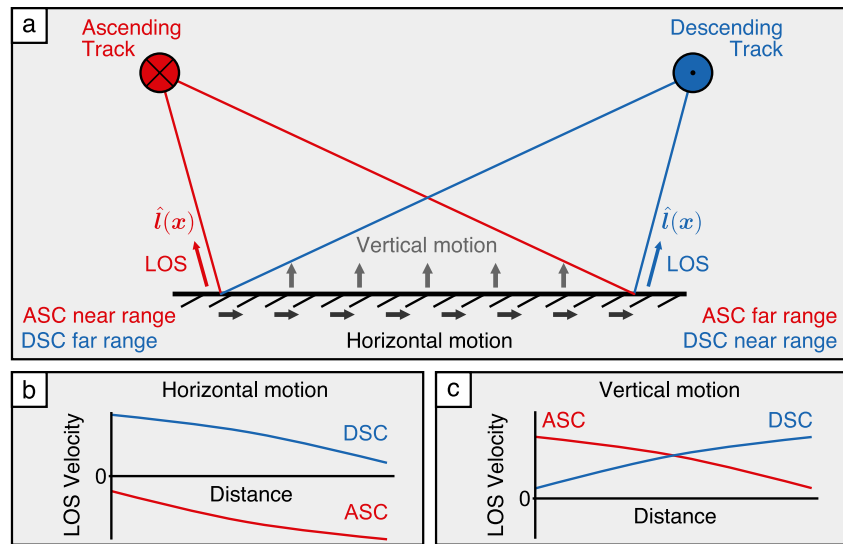
Figure 1. Illustration of how uniform horizontal and vertical motions result in ramps in Interferometric Synthetic Aperture Radar (InSAR) measurements. (a) Satellite acquires images in ascending (ASC) and descending (DSC) orbits, which have varying line-of-sight (LOS) incidence angles across the track. Red and blue arrows represent the LOS vector, $\hat{l}(\boldsymbol{x})$, for ASC and DSC orbits, respectively. Gray and black arrows represent plate motion in the reference frame of the satellite. For illustration purposes, we assume the ASC and DSC tracks are parallel to each other but in opposite directions, and ignore Earth's curvature. Figure not to scale. (b) Profile of the horizontal plate velocity projected into the LOS of the ASC and DSC tracks, against geographic distance along the ground. (c) Same as (b), except for vertical plate motion, resulting in opposite gradients in the LOS profiles. The observing geometry creates a small curvature in all profiles, which is exaggerated in the figure. InSAR measures LOS velocity relative to a reference point, which is equivalent to vertically shifting these profiles to intersect with the x axis at this point.

of rigid plate motion across the scene. We must therefore consider how velocities in ITRF appear in the InSAR deformation field. We represent the 3D ITRF secular velocity field of the Earth's surface as:

$$\boldsymbol{v}(\boldsymbol{x}) = \boldsymbol{v}_p(\boldsymbol{x}) + \boldsymbol{v}_d(\boldsymbol{x}), \tag{1}$$

where $\boldsymbol{v}_p(\boldsymbol{x})$ is the velocity field due to the strain-free motion of the relevant rigid plate in ITRF, and $\boldsymbol{v}_d(\boldsymbol{x})$ is the velocity due to internal deformation of the plate, for example, due to tectonic, volcanic, or hydrological processes. Defining the LOS unit vector pointing from the ground to the satellite as $\hat{l}(\boldsymbol{x})$ (Figure 1), the LOS projection of the 3D velocity field, minus the InSAR reference velocity, can be written as:

$$\boldsymbol{v}_l(\boldsymbol{x}) = \boldsymbol{v}(\boldsymbol{x}) \cdot \hat{l}(\boldsymbol{x}) - \boldsymbol{v}(\boldsymbol{x_0}) \cdot \hat{l}(\boldsymbol{x_0}), \tag{2}$$

where the reference is at point $\boldsymbol{x_0}$. $\boldsymbol{v}_l(\boldsymbol{x})$ is the secular velocity that will be measured by the satellite, assuming all other signals and noise can be neglected. In ITRF, $\boldsymbol{v}_l(\boldsymbol{x})$ has a contribution from the plate motion, which we can write as:

$$\boldsymbol{v}_{l,p}(\boldsymbol{x}) = \boldsymbol{v}_p(\boldsymbol{x}) \cdot \hat{l}(\boldsymbol{x}) - \boldsymbol{v}_p(\boldsymbol{x_0}) \cdot \hat{l}(\boldsymbol{x_0}). \tag{3}$$

The second term, from the reference, is constant, while the first term depends on the spatial variation of $\boldsymbol{v}_p(\boldsymbol{x})$ and $\hat{l}(\boldsymbol{x})$. The LOS vector $\hat{l}(\boldsymbol{x})$ can vary substantially over an image swath. For Sentinel-1, the incidence angle (the angle between the LOS and the vertical) varies approximately from 29° in the near range to 46° in the far range over the 250 km width of the imaging swath (for data acquired in Interferometric Wideswath mode). The range-dependent variation in $\hat{l}(\boldsymbol{x})$ implies a changing sensitivity to components of the 3D deformation field across the track, with sensitivity to horizontal motion increasing and vertical motion decreasing as we move from near range to far range. This range-dependent sensitivity causes uniform plate motions to appear as velocity ramps in the range direction when projected into the satellite LOS (Figure 1).

The plate velocity, $\boldsymbol{v}_p(\boldsymbol{x})$, also varies over an image swath. The motion of a rigid plate on Earth's surface can be represented by a rotation rate about an axis, known as an Euler pole (McKenzie & Parker, 1967). Given the

angular velocity of a chosen plate, $\mathbf{\Omega}$, we can write the linear velocity vector of any point on that plate with location vector $\boldsymbol{x}$ as $\boldsymbol{v}_p(\boldsymbol{x}) = \mathbf{\Omega} \times \boldsymbol{x}$, where $\times$ is the cross product. The amplitude and direction of the velocity field due to rigid plate motion therefore varies with distance from the plate's Euler pole, leading to a variation in the LOS velocity $\boldsymbol{v}_{l,p}(\boldsymbol{x})$.

Because of the effect of plate motion, InSAR velocity measurements should not generally be considered to be in a reference frame moving with the reference point. Choosing a reference point within an InSAR image offsets InSAR velocity measurements from the LOS projection of ITRF velocities by an unknown constant (Equation 1), but does not remove the long-wavelength gradients that can be induced by plate motion (Equation 3). The InSAR velocity gradient induced by rigid plate motion will be negligible $((\boldsymbol{v}_{l,p}(\boldsymbol{x}) \approx$ constant) if:

1. The plate motion does not vary substantially in space ($\boldsymbol{v}_p(\boldsymbol{x}) \approx$ constant), and
2. The magnitude of plate motion is small ($\boldsymbol{v}_p(\boldsymbol{x}) \approx 0$), or satellite LOS variation is negligible $(\hat{l}(\boldsymbol{x}) \approx 0)$.

Under these conditions, choosing a reference point that is stable with respect to the plate is then approximately equivalent to putting the InSAR velocities into the reference frame of that plate; however, this should not be generally assumed.

3. Data and Methods

3.1. Data Processing

We demonstrate the impact of plate motions using six tracks of InSAR data from the ESA's Sentinel-1 satellites, taken from ascending (ASC) and descending (DSC) orbits covering the Makran subduction zone (Iran), the Gulf of Aqaba (at the northern end of the Red Sea), and western Australia. For each track, we process at least 5 years of data using the InSAR Scientific Computing Environment (ISCE) (Fattahi, Agram, & Simons, 2017; Rosen et al., 2012) with enhanced spectral diversity for precise coregistration in the azimuth direction. After forming the interferogram networks, we create deformation time series using the small baseline approach as implemented in MintPy (Berardino et al., 2002; Yunjun et al., 2019).

Before examining residual signals due to plate motion, we apply corrections for the ionosphere, troposphere, SET, and topographic residuals due to potential DEM errors. We use split-band processing to correct for the ionosphere (Liang et al., 2019), PyAPS and the ERA5 weather model to mitigate the tropospheric delay (Hersbach et al., 2020; Jolivet et al., 2014), the method of Fattahi and Amelung (2013) for topographic residuals correction and PySolid to correct for SET (Milbert, 2018; Yunjun et al., 2022). Further details of our data and processing are presented in Supporting Information S1 (Text S1, S2, and Table S1).

3.2. Adjusting InSAR Measurements for Plate Motion

After all other corrections have been applied, we can then observe and account for the signal of plate motion. InSAR observations of ground motion are generally used to study regional deformation, rather than plate translations or rotations. For such purposes, a useful reference frame is one that moves with the plate in which we are trying to measure strain. Translating into this reference frame requires us to remove the signal of plate motion in the satellite's frame of reference, that is, ITRF (Bähr, 2013; Parizzi et al., 2020).

GNSS networks can be used to connect InSAR measurements to ITRF (e.g., Johnston et al., 2021; Mahapatra et al., 2018), which can then be transformed into a reference frame moving with the chosen plate. In the absence of sufficient GNSS coverage, we can estimate the transformation into the plate's frame of reference using the following steps:

1. Choose an InSAR reference point, $\boldsymbol{x_0}$, that is approximately stable with respect to the plate
2. Find the velocity field of the plate within ITRF, that is, $\boldsymbol{v}_p(\boldsymbol{x})$
3. Project that velocity field into the satellite LOS direction
4. Subtract the LOS velocity of the reference point, $\boldsymbol{v}_{l,p}(\boldsymbol{x_0})$, from the projected plate velocity to compute $\boldsymbol{v}_{l,p}(\boldsymbol{x})$, which is then removed from the InSAR velocity map.

Note that, after these steps, InSAR-derived velocities are still expressed relative to a reference point, meaning that deformation and other signals seen at the reference point will still affect the entire scene.

We use the geodetically constrained ITRF PMM of Altamimi et al. (2017) to estimate the plate velocity field. For each study region, we identify our reference plate (Table S1 in Supporting Information S1), then use the modeled secular angular velocity of the plate to calculate horizontal velocities for our observation region. We then project these velocities into the LOS direction and remove them from the velocity map.

4. Results

4.1. The Long-Wavelength Contributions From Other Signals

We expect plate motion to contribute below 8 mm/yr across the 250 km width of the Sentinel-1 tracks for our chosen regions (Figure S6 in Supporting Information S1), making it important to remove other signals to show what fraction of the residual velocity can be explained by plate motion. For ASC tracks in the Makran and Gulf of Aqaba, ionospheric corrections have a particularly large effect on the long-wavelength velocity signal (e.g., contributing a 25 mm/yr ramp along track 86 and a spatial standard deviation σ of 7.15 mm/yr for Makran, Figure 2), with DSC tracks showing substantially less ionospheric signal ($\sigma \approx 0.4$ mm/yr for track 20 in Makran and track 46 in Australia. Tables S2 and S3 in Supporting Information S1). ASC tracks are acquired at dusk—a period of greater ionosphere activity than dawn, when DSC tracks are acquired. This impact is still notable in C-band Sentinel-1 data, even though it suffers much less from ionospheric effects than L-band (Liang et al., 2019).

We find that troposphere corrections have a less significant impact on the long-wavelength velocity signal, in terms of the reduction in the spatial standard deviation σ ($\Delta\sigma \approx 10^{-1} - 1$ mm/yr. Figure 2k, Table S2 and S3 in Supporting Information S1), than the ionosphere for ASC tracks ($\Delta\sigma \approx 1 - 10^1$ mm/yr), and a comparable effect to ionosphere for DSC tracks ($\Delta\sigma \approx 10^{-1} - 1$ mm/yr). Corrections for the SET and topographic residuals have a small effect on the long-wavelength secular velocity ($\Delta\sigma \approx 10^{-2} - 10^{-1}$ mm/yr), contributing below 0.5 mm/yr over several hundred kilometers. We show the impact of the above corrections for all tracks in Figure 2 and Figures S1–S5 in Supporting Information S1, and present more details in Text S2 in Supporting Information S1. Figure 2l shows the effect of corrections in the temporal domain for a representative location. These time series highlight the removal of the strong ionospheric effect in the 2014–2016 period, and the substantial reduction in the seasonal tropospheric signal from the applied tropospheric model.

4.2. The Long-Wavelength Contribution From Plate Motion

After applying the suite of corrections we are left with residual velocity ramps in all of our tracks, predominantly in the range direction. We present the results of plate motion adjustments for several tracks in Figure 3. Our results show that accounting for plate motion removes a significant fraction of the residual velocity ramp in every case, reducing the across-track ramps from >2 to <0.5 mm/yr/100 km. The plate motion signal is larger than all other corrections to the long-wavelength velocity field, apart from the ionospheric delay in ASC tracks (Figure 2k).

The relative proximity of the Arabian plate Euler pole to the Aqaba region (Figure 3f) results in the plate velocity field varying appreciably within the tracks (Altamimi et al., 2017). This variation causes an additional LOS velocity ramp along the track, with an opposite direction for the ASC and DSC tracks. This along-track ramp results in a total plate motion ramp that deviates from the quasi-range direction (Figure 3a.iii and 3b.iii). Figures 3d.iv and 3e.iv show how this along-track gradient can be clearly seen in the profile and is well corrected for by the PMM, as seen in Figures 3d.v and 3e.v. We do not see similar along-track ramps for Australia and Makran, which is consistent with the plate motion velocity field.

5. Discussion

While other authors have noted the impact of plate motion (e.g., Bähr et al., 2012), the contribution of the ionosphere, orbital errors, and the troposphere, as well as the narrower swath of previous satellites have made it difficult to isolate. Recent advances in the quality and quantity of SAR data and correction methods, and the wide swath of Sentinel-1, allow us to isolate the plate motion signal and show the clear impact of accounting for it.
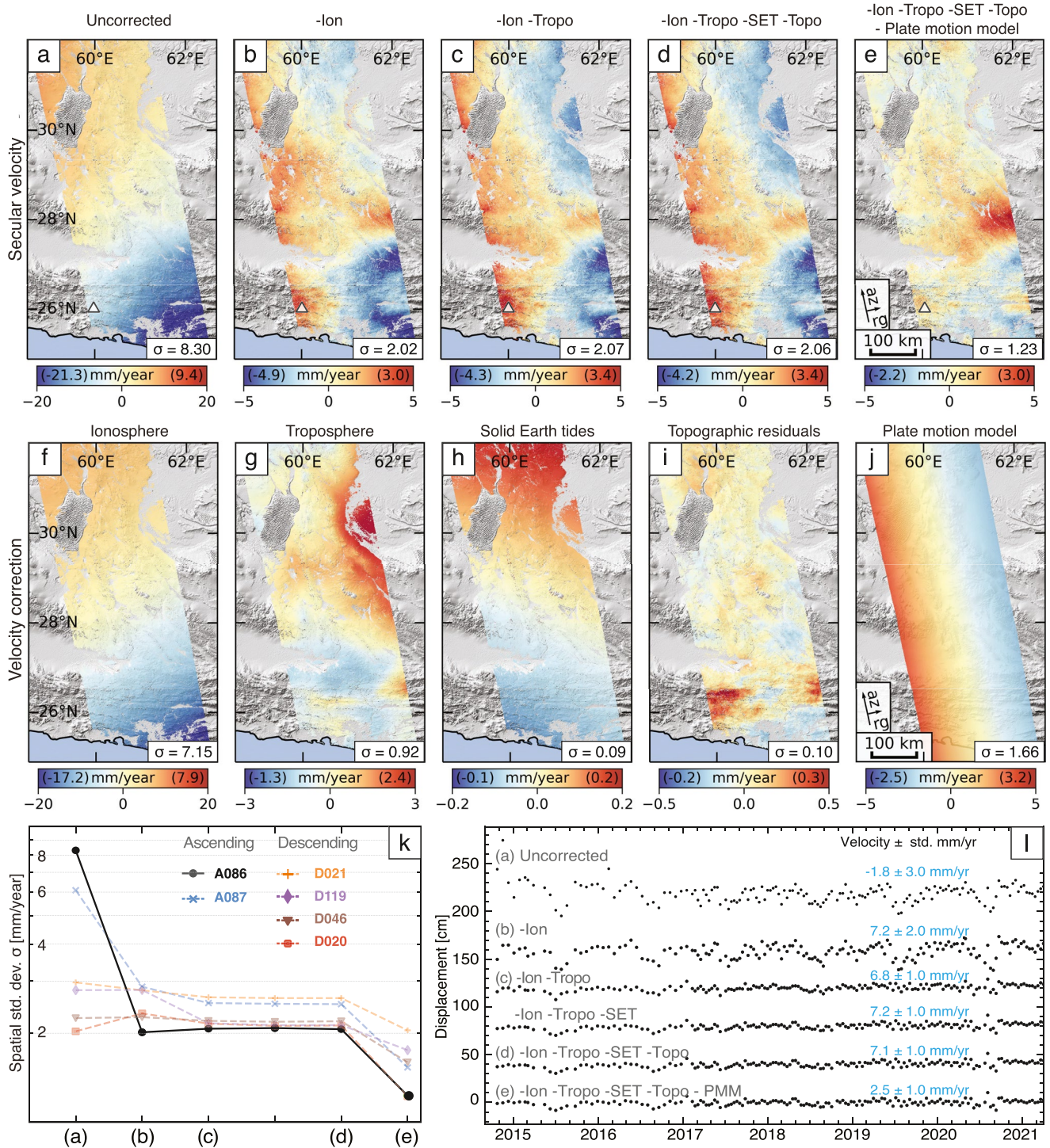
Figure 2. The cumulative impact of corrections on the Interferometric Synthetic Aperture Radar (InSAR) velocity for Sentinel-1 ASC track 86 over the Makran subduction zone. For plotting purposes, we remove the median value from each velocity field. Positive values represent apparent motion toward the satellite. Numbers in parentheses within the color bars refer to the 2.5 and 97.5 percentiles of the velocity. σ (mm/yr) denotes the spatial standard deviation of each field in mm/year. (a–e) Line-of-sight (LOS) velocities after each of the applied corrections. The triangle at (26°N, 60°E) marks the location of the time series in panel (l). The positive signal around (28°N, 62°E) in (e) is the post-seismic deformation from the 2013 Khash earthquake (Barnhart et al., 2014). (f–j) Apparent LOS velocities for each of the corrections. Larger signals in (i) in the south may be biases from topographic residual correction due to tropospheric turbulence (Fattahi & Amelung, 2013). (k) Spatial standard deviation σ as corrections are applied for each data set. (l) Time series at the triangle in (a–e), relative to a reference point at (32°N, 60°E), for track 86 after each correction stage.
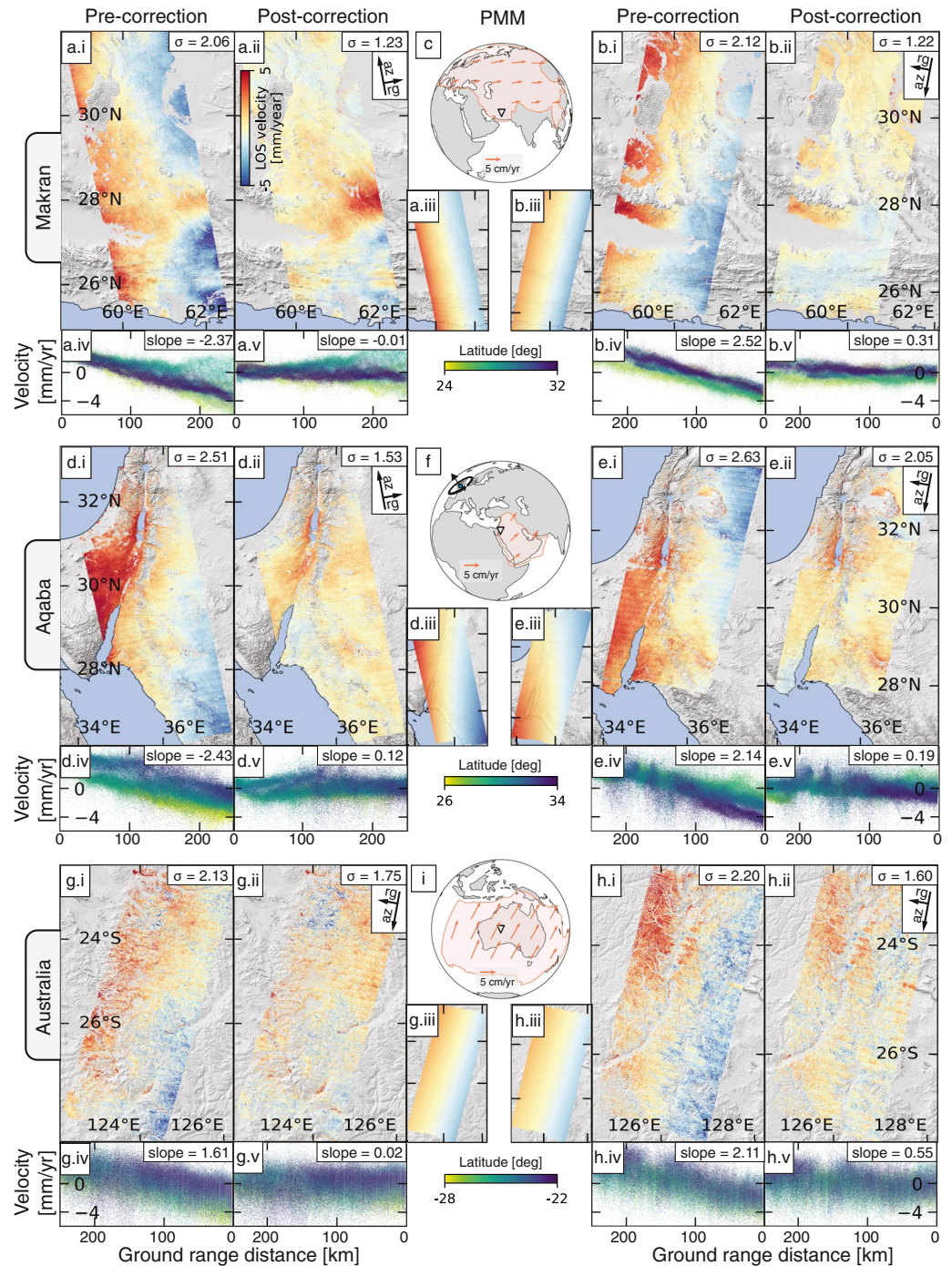
Figure 3. Plate motion adjustments for all tracks. All corrections except for plate motion model (PMM) have been applied. For plotting purposes, we remove the median from each velocity field. σ represents the spatial standard deviation of the velocity field (in mm/yr). (a and b) Makran ASC track 86 and DSC track 20, respectively. (c) Velocity field of the Eurasian plate from ITRF PMM for correction. The white triangle marks the location of (a and b). (i and ii) Velocity before and after PMM correction (iii). (iv and v) Velocity profile in range direction before and after PMM correction. The "slope" number in each profile represents the gradient of the linear least squares fit to the profile in mm/year/100 km, color-coded by latitude. (d–f) Similar to (a–c) but for the Gulf of Aqaba ASC track 87 and DSC track 21 with the Arabian plate use for correction. (g–i) Similar to (a–c) but for Australia DSC track 119 and 46 with the Australian plate used for correction.
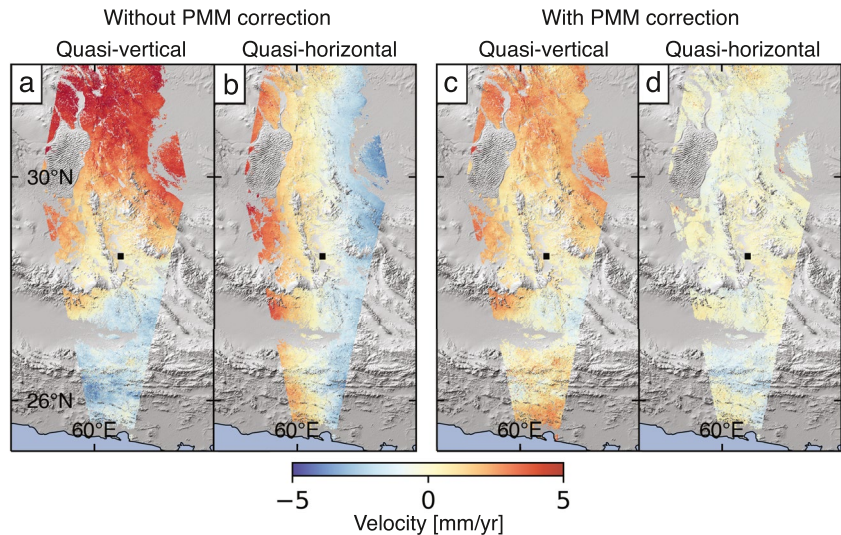
Figure 4. Bias in the decomposition for horizontal and vertical velocities from ASC (track 86) and DSC (track 20) tracks over the Makran subduction zone without plate motion model (PMM) correction, assuming purely east-west horizontal motion. The black square represents the reference point, which is assumed to be stationary with respect to the satellite. (a and b) Calculated vertical and eastward motion, respectively, before the PMM correction but after other corrections. (c and d) Same as (a and b) but with the PMM correction applied to each track before decomposition. Note that the biases in the long-wavelength velocity gradients in (a and b) have been substantially reduced by PMM correction.

When using InSAR for studying long-wavelength tectonic deformation, the most natural reference frame is one that is fixed to a stable region within the scene, so that we can interpret velocity gradients in terms of tectonic strain ($v_d(x)$ in Equation 1) rather than strain-free translation and rotation ($v_p(x)$ in Equation 1). There are several situations in which failing to account for the reference frame could bias the results (Figure 4):

1. Combining multiple tracks to estimate 3D deformation (Fialko et al., 2001; Wright et al., 2004). Plate motion can bias estimates of the 3D velocity field when we use an overlapping ASC and DSC track to calculate quasi-horizontal and quasi-vertical velocities (Figures 4a–4d and Text S4 in Supporting Information S1).
2. Modeling InSAR signals. If the long-wavelength signals in an InSAR velocity field are being modeled, and the model is assumed to not be rotating or translating, then a velocity ramp from plate motion may be modeled as strain accumulation and bias the results (e.g., changing the locking depth in a subduction zone model).
3. Comparisons between GNSS and InSAR. Both data sets must be in the same reference frame (Parizzi et al., 2020). If the GNSS are in a local reference frame, the InSAR and GNSS velocities will diverge at long wavelengths due to the signal of plate motion in the InSAR.

Studies that removed ramps from InSAR-derived velocities may have inadvertently mitigated the impact of plate motion in their observations, reducing the potential biases we outlined above.

Deficiencies in the PMM, or motion of the InSAR track reference point relative to the assumed plate, could also create long-wavelength residuals after plate motion correction. Motion relative to the plate will be of particular importance in areas of diffuse plate boundary deformation, where it is not possible to choose a reference point that is stable with respect to the rigid plate. This could be the case for tracks covering the Makran subduction zone and the Gulf of Aqaba, both of which span plate boundary zones. In these situations, plate motion models may not fully account for the impacts of distributed plate motion, and using local GNSS measurements to put InSAR measurements into a local terrestrial reference frame could be necessary (Bähr, 2013).

After adjusting for plate motion, remaining long-wavelength signals could be due to the incomplete removal of some signals (predominantly the troposphere (Fattahi & Amelung, 2015; Parizzi et al., 2021)) and orbital errors (Fattahi & Amelung, 2014), or actual strain accumulation in the lithosphere—the signal that InSAR measurements often target. See Text S2 in Supporting Information S1 for more details on the contributors to long-wavelength residuals. Other physical processes that could produce long-wavelength InSAR signals include ocean tidal loading, atmospheric, or longer-period hydrological loading. Such processes could introduce periodic

motions varying from 10^{-1} to 10^1 cm in amplitude (DiCaprio & Simons, 2008; Dong et al., 2002; Martens et al., 2016; Tregoning et al., 2009; Yu et al., 2020). The effects of these signals on InSAR decadal velocity fields are beyond the scope of this work.

The primary focus of this work is the impact of horizontal plate motions, and we have not considered the contribution of long-wavelength vertical velocities. Horizontal plate motions in ITRF are generally at the scale of centimeters per year (Altamimi et al., 2017), with long-wavelength vertical motions, for example, due to post-glacial rebound, significantly smaller at millimeters per year (e.g., Lau et al., 2020; Riddell et al., 2020). If an InSAR track is taken within a region that is experiencing constant vertical motion, this motion will also create a velocity ramp in the satellite LOS velocity field, but with ASC and DSC tracks having opposite gradients (Figure 1c). However, the amplitude of vertical velocities will result in smaller velocity gradients across the satellite track than those caused by horizontal motion (Text S3 and Figure S6 in Supporting Information S1).

6. Conclusion

We have illustrated how InSAR velocity measurements are sensitive to tectonic plate motion in the satellite reference frame. This motion will induce ramps in the InSAR velocity fields, predominantly in the satellite range direction, of up to several millimeters per year. In all of our multi-year time series, plate motion was the dominant long-wavelength signal after ionospheric and tropospheric corrections were applied. We have presented a simple adjustment method, which uses plate motion models to remove the plate motion signal from the InSAR velocity field. This adjustment substantially reduces long-wavelength ramps in multiple InSAR tracks from three different regions of the Earth. Routinely accounting for plate motion in InSAR could reduce biases when constraining long-wavelength tectonic strain induced by local geophysical phenomena. This correction is likely to be particularly useful where GNSS is not available to constrain the long-wavelength deformation. The signal of plate motion in InSAR data could also be used to improve plate motion models, which may be helpful where GNSS observations are sparse but high-quality InSAR data are available.

Data Availability Statement

The Sentinel-1 data were provided by the European Space Agency and downloaded from the Alaska Satellite Facility. InSAR data were processed using the InSAR Scientific Computing Environment (ISCE) (Rosen et al., 2012), available at https://github.com/isce-framework/isce2. Time series analysis was performed using the MintPy software (Yunjun et al., 2019), available at https://github.com/insarlab/MintPy. Our plate motion correction method is implemented in MintPy as plate_motion.py (https://github.com/insarlab/MintPy/blob/main/mintpy/plate_motion.py). Other data processing was performed using Python. Figures were produced using Matplotlib and Cartopy in Jupyter Notebooks, available at https://zenodo.org/record/6606282.

References

Agram, P. S., Jolivet, R., Riel, B., Lin, Y. N., Simons, M., Hetland, E., et al. (2013). New radar interferometric time series analysis toolbox released. *Eos, Transactions American Geophysical Union*, *94*(7), 69–70. https://doi.org/10.1002/2013EO070001

Altamimi, Z., Métivier, L., Rebischung, P., Rouby, H., & Collilieux, X. (2017). ITRF2014 plate motion model. *Geophysical Journal International*, *209*(3), 1906–1912. https://doi.org/10.1093/gji/ggx136

Altamimi, Z., Rebischung, P., Métivier, L., & Collilieux, X. (2016). ITRF2014: A new release of the International Terrestrial Reference Frame modeling nonlinear station motions. *Journal of Geophysical Research: Solid Earth*, *121*(8), 6109–6131. https://doi.org/10.1002/2016JB013098

Amelung, F., Galloway, D. L., Bell, J. W., Zebker, H. A., & Laczniak, R. J. (1999). Sensing the ups and downs of Las Vegas: InSAR reveals structural control of land subsidence and aquifer-system deformation. *Geology*, *27*(6), 483. https://doi.org/10.1130/0091-7613(1999)027<0483:stuado>2.3.co;2

Bähr, H. (2013). Orbital effects in spaceborne synthetic aperture radar interferometry (Doctoral dissertation). https://doi.org/10.5445/KSP/1000037166

Bähr, H., Samiei-Esfahany, S., & Hanssen, R. F. (2012). On the effect of reference frame motion on InSAR deformation estimates. In *Proceedings of Fringe 2011*. Retrieved from https://ui.adsabs.harvard.edu/abs/2012ESASP.697E..29B/abstract

Barnhart, W. D., Hayes, G. P., Samsonov, S. V., Fielding, E. J., & Seidman, L. E. (2014). Breaking the oceanic lithosphere of a subducting slab: The 2013 Khash, Iran earthquake. *Geophysical Research Letters*, *41*(1), 32–36. https://doi.org/10.1002/2013GL058096

Berardino, P., Fornaro, G., Lanari, R., & Sansosti, E. (2002). A new algorithm for surface deformation monitoring based on small baseline differential SAR interferograms. *IEEE Transactions on Geoscience and Remote Sensing*, *40*(11), 2375–2383. https://doi.org/10.1109/TGRS.2002.803792

Biggs, J., Wright, T., Lu, Z., & Parsons, B. (2007). Multi-interferogram method for measuring interseismic deformation: Denali Fault, Alaska. *Geophysical Journal International*, *170*(3), 1165–1179. https://doi.org/10.1111/j.1365-246X.2007.03415.x

Chaussard, E., Johnson, C. W., Fattahi, H., & Bürgmann, R. (2016). Potential and limits of InSAR to characterize interseismic deformation independently of GPS data: Application to the southern San Andreas Fault system. *Geochemistry, Geophysics, Geosystems*, *17*(3), 1214–1229. https://doi.org/10.1002/2015GC006246

Cong, X., Balss, U., Eineder, M., & Fritz, T. (2012). Imaging geodesy—Centimeter-level ranging accuracy with TerraSAR-X: An update. *IEEE Geoscience and Remote Sensing Letters*, *9*(5), 948–952. https://doi.org/10.1109/LGRS.2012.2187042

DiCaprio, C. J., & Simons, M. (2008). Importance of ocean tidal load corrections for differential InSAR. *Geophysical Research Letters*, *35*(22). https://doi.org/10.1029/2008gl035806

Doin, M. P., Lasserre, C., Peltzer, G., Cavalié, O., & Doubre, C. (2009). Corrections of stratified tropospheric delays in SAR interferometry: Validation with global atmospheric models. *Journal of Applied Geophysics*, *69*(1), 35–50. https://doi.org/10.1016/j.jappgeo.2009.03.010

Dong, D., Fang, P., Bock, Y., Cheng, M. K., & Miyazaki, S. (2002). Anatomy of apparent seasonal variations from GPS-derived site position time series. *Journal of Geophysical Research*, *107*(B4), 9–1. https://doi.org/10.1029/2001JB000573

Fattahi, H., Agram, P., & Simons, M. (2017). A network-based enhanced spectral diversity approach for TOPS time-series analysis. *IEEE Transactions on Geoscience and Remote Sensing*, *55*(2), 777–786. https://doi.org/10.1109/TGRS.2016.2614925

Fattahi, H., & Amelung, F. (2013). DEM error correction in InSAR time series. geoscience and remote sensing. *IEEE Transactions on*, *51*(7), 4249–4259. https://doi.org/10.1109/TGRS.2012.2227761

Fattahi, H., & Amelung, F. (2014). InSAR uncertainty due to orbital errors. *Geophysical Journal International*, *199*(1), 549–560. https://doi.org/10.1093/gji/ggu276

Fattahi, H., & Amelung, F. (2015). InSAR bias and uncertainty due to the systematic and stochastic tropospheric delay. *Journal of Geophysical Research: Solid Earth*, *120*(12), 8758–8773. https://doi.org/10.1002/2015JB012419

Fattahi, H., Simons, M., & Agram, P. (2017). InSAR time-series estimation of the ionospheric phase delay: An extension of the split range-spectrum technique. *IEEE Transactions on Geoscience and Remote Sensing*, *55*(10), 5984–5996. https://doi.org/10.1109/TGRS.2017.2718566

Fialko, Y. (2006). Interseismic strain accumulation and the earthquake potential on the southern San Andreas fault system. *Nature*, *441*(7096), 968–971. https://doi.org/10.1038/nature04797

Fialko, Y., Simons, M., & Agnew, D. (2001). The complete (3-D) surface displacement field in the epicentral area of the 1999 Mw 7.1 Hector Mine earthquake, California, from space geodetic observations. *Geophysical Research Letters*, *28*(16), 3063–3066. https://doi.org/10.1029/2001GL013174

Fournier, T., Pritchard, M. E., & Finnegan, N. (2011). Accounting for atmospheric delays in InSAR data in a search for long-wavelength deformation in South America. *IEEE Transactions on Geoscience and Remote Sensing*, *49*(10), 3856–3867. https://doi.org/10.1109/TGRS.2011.2139217

Gomba, G., Parizzi, A., De Zan, F., Eineder, M., & Bamler, R. (2016). Toward operational compensation of ionospheric effects in SAR interferograms: The split-spectrum method. *IEEE Transactions on Geoscience and Remote Sensing*, *54*(3), 1446–1461. https://doi.org/10.1109/TGRS.2015.2481079

Hanssen, R. F. (2001). *Radar interferometry: Data interpretation and error analysis* (Vol. 2). Springer Netherlands. https://doi.org/10.1007/0-306-47633-9

Hersbach, H., Bell, B., Berrisford, P., Hirahara, S., Horányi, A., Muñoz-Sabater, J., et al. (2020). The ERA5 global reanalysis. *Quarterly Journal of the Royal Meteorological Society*, *146*(730), 1999–2049. https://doi.org/10.1002/qj.3803

Hooper, A., Bekaert, D., Spaans, K., & Arikan, M. (2012). Recent advances in SAR interferometry time series analysis for measuring crustal deformation. *Tectonophysics*, *514–517*, 1–13. https://doi.org/10.1016/j.tecto.2011.10.013

Johnston, P. J., Filmer, M. S., & Fuhrmann, T. (2021). Evaluation of methods for connecting InSAR to a terrestrial reference frame in the Latrobe Valley, Australia. *Journal of Geodesy*, *95*(10), 115. https://doi.org/10.1007/s00190-021-01560-2

Jolivet, R., Agram, P. S., Lin, N. Y., Simons, M., Doin, M.-P., Peltzer, G., & Li, Z. (2014). Improving InSAR geodesy using global atmospheric models. *Journal of Geophysical Research: Solid Earth*, *119*(3), 2324–2341. https://doi.org/10.1002/2013JB010588

Jolivet, R., Grandin, R., Lasserre, C., Doin, M. P., & Peltzer, G. (2011). Systematic InSAR tropospheric phase delay corrections from global meteorological reanalysis data. *Geophysical Research Letters*, *38*(17), 1–6. https://doi.org/10.1029/2011GL048757

Jolivet, R., Simons, M., Agram, P. S., Duputel, Z., & Shen, Z.-K. (2015). Aseismic slip and seismogenic coupling along the central San Andreas Fault. *Geophysical Research Letters*, *42*(2), 297–306. https://doi.org/10.1002/2014GL062222

Lau, N., Borsa, A. A., & Becker, T. W. (2020). Present-day crustal vertical velocity field for the contiguous United States. *Journal of Geophysical Research: Solid Earth*, *125*(10). https://doi.org/10.1029/2020JB020066

Lazecky, M., & Hooper, A. (2022). *InSAR-derived horizontal velocities in a global reference frame* (pp. 1–14). ESSOAr. https://doi.org/10.1002/essoar.10511058.1

Li, Z., Muller, J. P., Cross, P., & Fielding, E. J. (2005). Interferometric synthetic aperture radar (InSAR) atmospheric correction: GPS, moderate resolution imaging spectroradiometer (MODIS), and InSAR integration. *Journal of Geophysical Research*, *110*(3), 1–10. https://doi.org/10.1029/2004JB003446

Liang, C., Agram, P., Simons, M., & Fielding, E. J. (2019). Ionospheric correction of InSAR time series analysis of C-band Sentinel-1 TOPS Data. *IEEE Transactions on Geoscience and Remote Sensing*, *57*(9), 6755–6773. https://doi.org/10.1109/tgrs.2019.2908494

Mahapatra, P., der Marel, H. V., van Leijen, F., Samiei-Esfahany, S., Klees, R., & Hanssen, R. (2018). InSAR datum connection using GNSS-augmented radar transponders. *Journal of Geodesy*, *92*(1), 21–32. https://doi.org/10.1007/s00190-017-1041-y

Marinkovic, P., & Larsen, Y. (2015). On resolving the local oscillator drift induced phase ramps in ASAR and ERS1/2 interferometric data—The final solution. In *Fringe 2015 workshop (ESA SP - 731)* (Vol. *1*), 20.

Martens, H. R., Simons, M., Owen, S., & Rivera, L. (2016). Observations of ocean tidal load response in South America from subdaily GPS positions. *Geophysical Journal International*, *205*(3), 1637–1664. https://doi.org/10.1093/gji/ggw087

Massonnet, D., & Feigl, K. L. (1998). Radar interferometry and its application to changes in the Earth's surface. *Reviews of Geophysics*, *36*(4), 441–500. https://doi.org/10.1029/97RG03139

Massonnet, D., Rossi, M., Carmona, C., Adragna, F., Peltzer, G., Feigl, K., & Rabaute, T. (1993). The displacement field of the Landers earthquake mapped by radar interferometry. *Nature*, *364*(6433), 138–142. https://doi.org/10.1038/364138a0

McKenzie, D. P., & Parker, R. L. (1967). The North Pacific: An example of tectonics on a sphere. *Nature*, *216*(5122), 1276–1280. https://doi.org/10.1038/2161276a0

Merryman Boncori, J. P. (2019). Measuring coseismic deformation with spaceborne synthetic aperture radar: A review. *Frontiers of Earth Science*, *7*, 1–20. https://doi.org/10.3389/feart.2019.00016

Milbert, D. (2018). Solid: Solid earth tide. Retrieved from https://geodesyworld.github.io/SOFTS/solid.htm

Morishita, Y., Lazecky, M., Wright, T., Weiss, J., Elliott, J., & Hooper, A. (2020). LiCSBAS: An open-source InSAR time series analysis package integrated with the LiCSAR automated Sentinel-1 InSAR Processor. *Remote Sensing*, *12*(3), 424. https://doi.org/10.3390/rs12030424

Neely, W. R., Borsa, A. A., & Silverii, F. (2020). GInSAR: A cGPS correction for enhanced InSAR time series. *IEEE Transactions on Geoscience and Remote Sensing*, *58*(1), 136–146. https://doi.org/10.1109/TGRS.2019.2934118

Parizzi, A., Brcic, R., & De Zan, F. (2021). InSAR performance for large-scale deformation measurement. *IEEE Transactions on Geoscience and Remote Sensing*, *59*(10), 8510–8520. https://doi.org/10.1109/TGRS.2020.3039006

Parizzi, A., Gonzalez, F. R., & Brcic, R. (2020). A covariance-based approach to merging InSAR and GNSS displacement rate measurements. *Remote Sensing*, *12*(2), 300. https://doi.org/10.3390/rs12020300

Peter, H. (2021). Copernicus POD product handbook: Copernicus Sentinel-1, -2 and -3 precise orbit determination service (CPOD). (Tech. Rep.). *GMV*. Retrieved from https://sentinel.esa.int/documents/247904/4599719/Copernicus-POD-Product-Handbook.pdf

Riddell, A. R., King, M. A., & Watson, C. S. (2020). Present-day vertical land motion of Australia from GPS observations and geophysical models. *Journal of Geophysical Research: Solid Earth*, *125*(2). https://doi.org/10.1029/2019JB018034

Rosen, P. A., Gurrola, E., Sacco, G. F., & Zebker, H. (2012). The InSAR scientific computing environment. In *Proceedings of the European Conference on Synthetic Aperture Radar* (Vol. 2012, pp. 730–733). EUSAR.

Simons, M., & Rosen, P. (2015). Interferometric synthetic aperture radar geodesy. In *Treatise on geophysics* (Vol. 3, pp. 339–385). Elsevier. https://doi.org/10.1016/B978-0-444-53802-4.00061-0

Tarayre, H., & Massonnet, D. (1996). Atmospheric propagation heterogeneities revealed by ERS-1 interferometry. *Geophysical Research Letters*, *23*(9), 989–992. https://doi.org/10.1029/96GL00622

Tregoning, P., Watson, C., Ramillien, G., McQueen, H., & Zhang, J. (2009). Detecting hydrologic deformation using GRACE and GPS. *Geophysical Research Letters*, *36*(15). https://doi.org/10.1029/2009gl038718

Weiss, J. R., Walters, R. J., Morishita, Y., Wright, T. J., Lazecky, M., Wang, H., et al. (2020). High-resolution surface velocities and strain for Anatolia from sentinel-1 InSAR and GNSS data. *Geophysical Research Letters*, *47*(17). https://doi.org/10.1029/2020GL087376

Wright, T. J., Parsons, B. E., & Lu, Z. (2004). Toward mapping surface deformation in three dimensions using InSAR. *Geophysical Research Letters*, *31*(1), 1–5. https://doi.org/10.1029/2003GL018827

Xu, X., & Sandwell, D. T. (2020). Toward absolute phase change recovery with InSAR: Correcting for Earth tides and phase unwrapping ambiguities. *IEEE Transactions on Geoscience and Remote Sensing*, *58*(1), 726–733. https://doi.org/10.1109/TGRS.2019.2940207

Xu, X., Sandwell, D. T., Klein, E., & Bock, Y. (2021). Integrated Sentinel-1 InSAR and GNSS time-series along the San Andreas fault system. *Journal of Geophysical Research: Solid Earth*, *126*(11), 1–14. https://doi.org/10.1029/2021JB022579

Xu, Z.-W., Wu, J., & Wu, Z.-S. (2004). A survey of ionospheric effects on space-based radar. *Waves in Random Media*, *14*(2), S189–S273. https://doi.org/10.1088/0959-7174/14/2/008

Yu, C., Penna, N. T., & Li, Z. (2020). Ocean tide loading effects on InSAR Observations over wide regions. *Geophysical Research Letters*, *47*(15). https://doi.org/10.1029/2020GL088184

Yunjun, Z., Fattahi, H., & Amelung, F. (2019). Small baseline InSAR time series analysis: Unwrapping error correction and noise reduction. *Computers & Geosciences*, *133*, 104331. https://doi.org/10.1016/j.cageo.2019.104331

Yunjun, Z., Fattahi, H., Pi, X., Rosen, P., Simons, M., Agram, P., & Aoki, Y. (2022). Range geolocation accuracy of C-/L-band SAR and its implications for operational stack coregistration. *IEEE Transactions on Geoscience and Remote Sensing*, *2892*, 1–19. https://doi.org/10.1109/TGRS.2022.3168509

References From the Supporting Information

Altamimi, Z., Métivier, L., & Collilieux, X. (2012). ITRF2008 plate motion model. *Journal of Geophysical Research*, *117*(7), 1–14. https://doi.org/10.1029/2011JB008930

Ansari, H., De Zan, F., & Parizzi, A. (2021). Study of systematic bias in measuring surface deformation with SAR interferometry. *IEEE Transactions on Geoscience and Remote Sensing*, *59*(2), 1285–1301. https://doi.org/10.1109/TGRS.2020.3003421

Bekaert, D., Walters, R., Wright, T., Hooper, A., & Parker, D. (2015). Statistical comparison of InSAR tropospheric correction techniques. *Remote Sensing of Environment*, *170*, 40–47. https://doi.org/10.1016/j.rse.2015.08.035

Chen, C. W., & Zebker, H. A. (2002). Phase unwrapping for large SAR interferograms: Statistical segmentation and generalized network models. *IEEE Transactions on Geoscience and Remote Sensing*, *40*(8), 1709–1719. https://doi.org/10.1109/TGRS.2002.802453

De Zan, F., Parizzi, A., Prats-Iraola, P., & López-Dekker, P. (2014). A SAR interferometric model for soil moisture. *IEEE Transactions on Geoscience and Remote Sensing*, *52*(1), 418–425. https://doi.org/10.1109/TGRS.2013.2241069

Emardson, T. R., Simons, M., & Webb, F. H. (2003). Neutral atmospheric delay in interferometric synthetic aperture radar applications: Statistical description and mitigation. *Journal of Geophysical Research*, *108*(B5), 1–8. https://doi.org/10.1029/2002JB001781

Li, Z., Wright, T., Hooper, A., Crippa, P., Gonzalez, P., Walters, R., et al. (2016). Towards InSAR everywhere, all the time, with Sentinel-1. International archives of the photogrammetry. *Remote Sensing and Spatial Information Sciences - ISPRS Archives*, *41*, 763–766. https://doi.org/10.5194/isprsarchives-XLI-B4-763-2016

Petit, G., & Luzum, B. (2010). IERS conventions (IERS technical note No. 36). Retrieved from http://www.iers.org/TN36/

Zebker, H. A., & Villasenor, J. (1992). Decorrelation in interferometric radar echoes. *IEEE Transactions on Geoscience and Remote Sensing*, *30*(5), 950–959. https://doi.org/10.1109/36.175330

Zheng, Y., Fattahi, H., Agram, P., Simons, M., & Rosen, P. (2022). On closure phase and systematic bias in multilooked SAR interferometry. *IEEE Transactions on Geoscience and Remote Sensing*, *60*, 1–11. https://doi.org/10.1109/TGRS.2022.3167648